Physics-informed data-driven geometric accuracy prediction for hemisphere structures produced by two-photon lithography

Sixian Jia[1] Jieliyue Sun[2] Andrew Howes[2] Michelle R. Dawson[3] Kimani C. Toussaint Jr.[2]
Chenhui Shao[1]

[1]*Department of Mechanical Science and Engineering, University of Illinois at Urbana-Champaign, Urbana, IL 61801, USA*
[2]*School of Engineering, Brown University, Providence, RI 02912, USA*
[3]*Department of Molecular Biology, Cell Biology, and Biochemistry, Brown University, Providence, RI 02912, USA*

Abstract

Two-photon lithography (TPL) is an additive manufacturing technique to produce three-dimensional (3D) micro- and nano-scale structures. Geometric compliance is of vital importance to ensure the quality and functionality of additively manufactured 3D structures. However, there exists limited research on modeling and predicting the geometric compliance of TPL. This paper presents a new generalizable physics-informed, data-driven modeling framework for cross-design and cross-parameter geometric accuracy prediction. A large-scale experimental design consisting of six hemisphere sizes and six parameter combinations is carried out to thoroughly test the effectiveness of the proposed method. It is shown that the modeling framework is highly effective in predicting the geometric accuracy for a previously unseen scenario with knowledge derived from other designs and parameters. The average prediction errors for radius and height, which are key geometric features of hemispheres, are 5.23% and 4.66%, respectively. To the best of our knowledge, this study is among the first to develop a generalizable method for cross-design and cross-parameter geometric accuracy modeling in TPL.

1. Introduction

Two-photon lithography (TPL), also referred to as direct laser writing, is an additive manufacturing (AM) technique to fabricate three-dimensional (3D) micro and nanostructures [1, 2]. In a typical TPL process, a femtosecond laser beam is focused tightly onto a photopolymer resist. The peak intensity at the focal point leads photoinitiators to reach the excited state by absorption of two photons simultaneously, causing the depolymerization of the resist [3]. TPL process parameters, such as the average power of the femtosecond laser, exposure time, and numerical aperture of the objective influence the resolution of TPL based on the scaling laws [4].

3D micro/nanostructures have numerous promising applications in the fields of micro-optics, mechanical metamaterials, electronics, and bio-scaffolds [5]. The miniaturization and integration of structures necessitate high geometric compliance [6]. While it has been demonstrated to fabricate various complex 3D structures in prototyping applications, the precision and resolution of TPL have not been adequately investigated, raising concerns about its utility in scalable production [7].

Some recent studies have been focused on the geometric compliance of TPL. Zhou et al. [8] discussed the factors that may affect the accuracy of TPL such as laser power, scanning rate, and the choice of photoresist material, and suggested methods to improve the processing accuracy, including radical quencher, multipath scanning method, and shape precompensation. Yang et al. developed a modeling and decision–making framework that uses Gaussian process regression to model the spatial geometric variability of TPL-fabricated structures [7]. A data-driven compensation algorithm was developed to minimize the geometric errors. The same TPL process parameters and structure designs were used in this work, but the generalizability to other scenarios is unclear.

This paper develops a physics-informed data-driven framework to predict the geometric accuracy of TPL-fabricated 3D structures across different process parameters and different structure dimensions, with a focus on hemisphere structures. The framework is informed by physics and derived based on the voxel dimension models. It is discovered that the parameters of the structure-level model are strongly linearly related to the design dimension, which enables predictive and generalizable modeling across designs and parameters. Experimental results show that the proposed approach permits high prediction accuracy—the average prediction errors for radius and height are 5.23% and 4.66%, respectively.

The remainder of this paper is organized as follows. The design of experiments is shown in Section 2. Section 3 presents the details of the modeling framework. Section 4 discusses the prediction results and demonstrates the effectiveness the modeling framework. Finally, Section 5 concludes the paper.

2. Design of Experiments

To demonstrate the effectiveness of the proposed modeling method, we designed TPL experiments with varied process parameters and hemisphere dimensions. Section 2.1 presents the details of the experimental design and fabrication. The procedure of geometric measurement is discussed in Section 2.2.

2.1. Design and fabrication

Experiments were conducted by varying (1) the hemisphere radius and (2) TPL process parameters including the laser power (LP) and the scanning rate (SR). While other process parameters may also influence the geometric accuracy in TPL, they were kept as constant in this study and will be investigated in future research. The design of experiments is illustrated by Fig. 1. The radius of the hemisphere was varied from 1.6 µm to 2.6 µm with a 0.2-µm increment. Six combinations of LP and SR, which are referred to as P1–P6, were used to fabricate prescribed hemisphere designs. Table 1 provides the details of the parameters. Dose, which is approximately proportional to $\frac{LP^2}{SR}$, is also calculated for each parametric combination. It is reported that dose is an important factor that influences the fabricated structure quality [1, 9]. Dose can be increased by raising the laser power or extending the duration that the focal spot remains in a fixed position, accomplished through adjustments in either scan speed or exposure time. For each parametric combination, a *group* of 20 samples were fabricated in a 4 by 5 sample array. Each *sample* consisted of 25 structures that were evenly placed in a 5 by 5 array. Therefore, 3,000 structures were fabricated for each design. The total number of structures is 18,000.
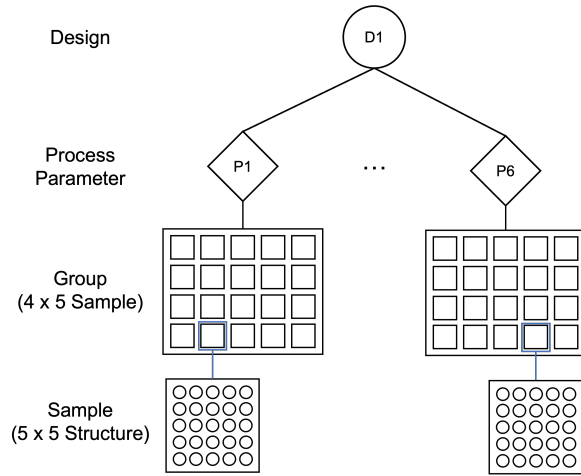

Fig. 1. Experiments were repeated for hemisphere radius design (D1–D6) of 1.6 µm, 1.8 µm, 2.0 µm, 2.2 µm, 2.4 µm, and 2.6 µm. Six parametric combinations (P1–P6) were used for each design. 20 samples were fabricated for each parametric combination, forming a "Group." One sample consists of 25 hemisphere structures placed in a 5 by 5 array.

Photonic Professional (Nanoscribe, GT) 3D printer was used to manufacture the structures. The printer is equipped with a pulsed femtosecond fiber laser emitting at a center wavelength of 780 nm. 0.05 ml of photoresist (IP-Dip) was applied onto a 1 in × 1 in fused silica substrate. The numerical aperture of the objective is 1.4 and the magnification is 63×. The default setting for the power scale is 1.0 and the reference power at our objective aperture, which is 50 mW.

Table 1
Parametric combinations used in the experiments.

Group	LP (%)	SR (mm/s)	Dose
P1	50	40	62.50
P2	50	60	41.67
P3	55	60	50.42
P4	50	55	45.45
P5	50	50	50.00
P6	50	45	55.56

2.2. Geometric measurement

A 3D laser scanning microscope (KEYENCE, VK-X1000) was used for structure measurements. The height measurement for each sample was stored in the format of a 768 × 1024 matrix. Equivalent radius and average height are two important geometric features characterizing hemispheres. An image processing algorithm is created to automatically calculate the geometric features from the 3D measurements. The equivalent radius is calculated from counting the number of pixels within the surface area. Taking the average of the height values from the flat surface area generates the average height of one structure. The ideal average height value of a hemisphere is equal to $\frac{2}{3}$ times the designed radius.

3. Geometric Accuracy Modeling

In this section, we first derive models for equivalent radius (R) and average height (H) from the physics-based voxel dimension models in Section 3.1. Section 3.2 presents the linear relationships between the model parameters and design dimensions, based on which generalizable models are derived.

3.1. Structure-level model

The voxel diameter and voxel length can be calculated by

$$d(\mathrm{LP}, \mathrm{SR}) = m_d \left[\ln \left(n_d \frac{\mathrm{LP}^2}{\mathrm{SR}} \right) \right]^{\frac{1}{2}}, \quad (1)$$

$$l(\mathrm{LP}, \mathrm{SR}) = m_l \left[\left(n_l \frac{\mathrm{LP}^2}{\mathrm{SR}} \right)^{\frac{1}{2}} - 1 \right]^{\frac{1}{2}}, \quad (2)$$

where m_d, n_d, m_l, and n_l are combinations of multiple physical variables.

The fabrication of the structures is reliant on the stack of voxels. Therefore, the geometric compliance of these structures is influenced by the resolution and spatial arrangement of the voxels. Equivalent radius and average height, which are measured in x and z directions, respectively, are directly related to voxel diameter and length.

Based on Eqs. (1) and (2), we add a constant number to each model to improve the flexibility and capability of modeling. As such, the R model and H model can be expressed as

$$\mathrm{R}(\mathrm{LP}, \mathrm{SR}) = a_R \left[\ln \left(b_R \frac{\mathrm{LP}^2}{\mathrm{SR}} \right) \right]^{\frac{1}{2}} + c_R, \quad (3)$$

$$H(\mathrm{LP}, \mathrm{SR}) = a_H \left[\left(b_H \frac{\mathrm{LP}^2}{\mathrm{SR}} \right)^{\frac{1}{2}} - 1 \right]^{\frac{1}{2}} + c_H. \qquad (4)$$

The parameters $a_{(\cdot)}$, $b_{(\cdot)}$, and $c_{(\cdot)}$ can be estimated using gradient descent method. This algorithm moves the parameters in the direction of steepest descent, which allows it to reach a local minimum or saddle point of the function. The loss is defined as mean square error for the gradient descent process. The minimum requirement for estimating the parameters is using one combination of LP and SR for one design.

Mean absolute percentage error (MAPE) is used as an evaluation metric to examine the modeling performance. MAPE measures the average magnitude of deviations between predictions and actual values, which can help us understand the percentage offset compared with the ground truth. In this work, MAPE is more suitable than other metrics such as root mean square error and mean absolute error because we have diverse hemisphere dimensions. We use the cross validation method to train on data from five parameter groups (folds) and test on the remaining group (fold) for each design. In each cross-validation run, the sizes of training and test sets are 2,500 and 500, respectively. The results are reported in Table 2. The training and test MAPE values are less than 5% for both R and H models and the models do not suffer from overfitting issues.

Table 2
Modeling performance for R and H models.

	Training MAPE (%)	Test MAPE (%)
R	3.585	4.166
H	3.780	4.473

3.2. Generalizable cross-design modeling

Cross-design modeling aims to build a predictive model for a new design only using measurement data from other designs. This requires high generalization capability. We approach this problem by studying the relationship of the sets of (a,b,c) in Eqs. (3) and (4) among different designs. The parameters (a,b,c) vs. designs for R and H models are visualized in Fig. 2. All plots exhibit approximately linear trends and the coefficient of determination R^2 between designed radius D and parameter value nearly equals 1 for all parameters. It is also noticed that all the parameters linearly increase as D increases.

The strong linear correlations between the parameters (a, b, c) and D shown in Fig. 2 allow us to derive linear predictive models as

$$a_{(\cdot)} = \beta_{a_{(\cdot)0}} \times D + \beta_{a_{(\cdot)1}}, \qquad (5)$$

$$b_{(\cdot)} = \beta_{b_{(\cdot)0}} \times D + \beta_{b_{(\cdot)1}}, \qquad (6)$$

$$c_{(\cdot)} = \beta_{c_{(\cdot)0}} \times D + \beta_{c_{(\cdot)1}}, \qquad (7)$$

where $\beta_{(\cdot)0}$ and $\beta_{(\cdot)1}$ are the slope and the intercept of the linear models, respectively; and $(\cdot)$ can be R or H. $\theta(\cdot)$ is used to represent the parameter set $(a_{(\cdot)}, b_{(\cdot)}, c_{(\cdot)})$ and $\beta(\cdot)$ denotes $(\beta_{(\cdot)0}, \beta_{(\cdot)1})$.

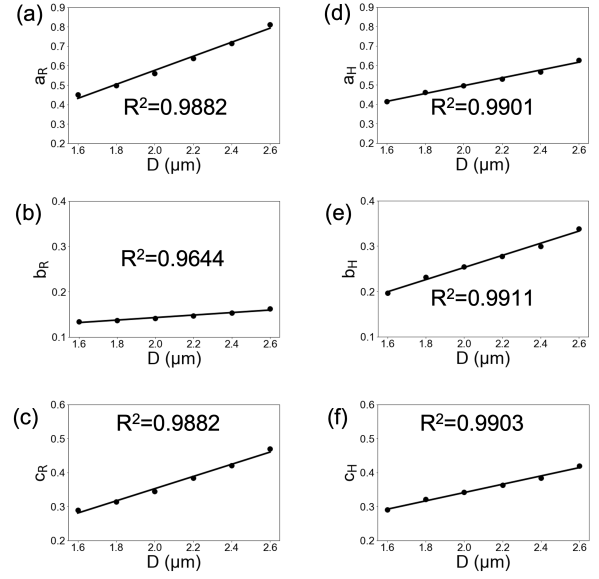Eqs. (5)–(7) enable cross-design and cross-parameter predictive modeling in a highly generalizable

Fig. 2. The relationship between the parameters of geometric features and designed radius value: (a) a_R, (b) b_R, (c) c_R, (d) a_H, (e) b_H, (f) c_H.

way. In each equation, the parameters to be estimated are slope and intercept, i.e., $\beta(\cdot)$. Therefore, the minimum requirement for estimating all parameters in these equations is that measurements of two designs with one parameter group are available. Once Eqs. (5)–(7) are available, one can obtain θ_* for a previously unseen design D_*, which are subsequently used to obtain models Eqs. (3) and (4). Using Eqs. (3)–(7), we can accurately predict the expected values for geometric features given an arbitrary design using the modeling framework that is illustrated by Fig. 3.
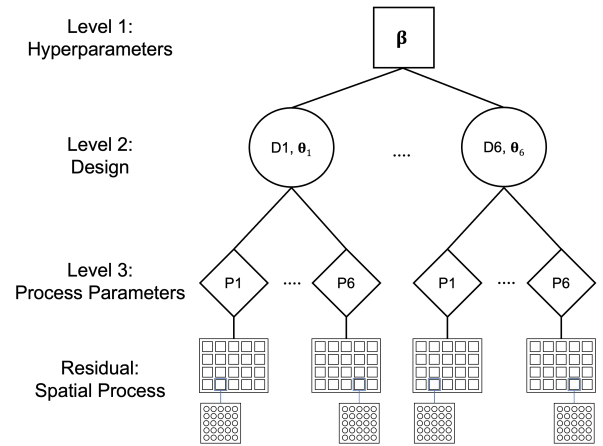

Fig. 3. Overview of the generalizable modeling framework.

The expected geometric features are determined by the parameter set (LP, SR; D). Further, the relationship between (LP, SR) and R or H is determined by D. Therefore, β serves as hyperparameters from the perspective of statistical learning or machine learning. Knowledge transfer or generalizability is supported by the fact that

one can obtain the relationship between (LP, SR) and R or H using knowledge from other designs.

4. Results

In this section, we design a two-way cross-validation (2CV) method to test the performance and generalizability of the model developed in Section 3.2. The full dataset is split into training and test sets. In the training phase, the model has no access to data with the same process parameters or designs that exist in the test dataset, highlighting a challenging, generalizable learning scenario. The full data is split into 6×6 folds. Each fold includes 500 data points. In each of the 36 2CV runs, the combination of $D_i P_j$ ($i = 1, \ldots, 6$, $j = 1, \ldots, 6$) is selected as the test set and the training set consists of 25 folds without D_i or P_j. The sizes of training and test datasets are 12,500 and 500, respectively.

We apply the 2CV method to all 36 folds of data to evaluate the R and H models. The average test MAPE values for R model and H model are 5.23% and 4.66%, respectively. The test MAPE values are reported in Fig. 4 and Fig. 5, grouped by design and parameter group, respectively. It is seen that the test MAPEs stay at a low level across designs and parameters, indicating robust performance and good generalizability.
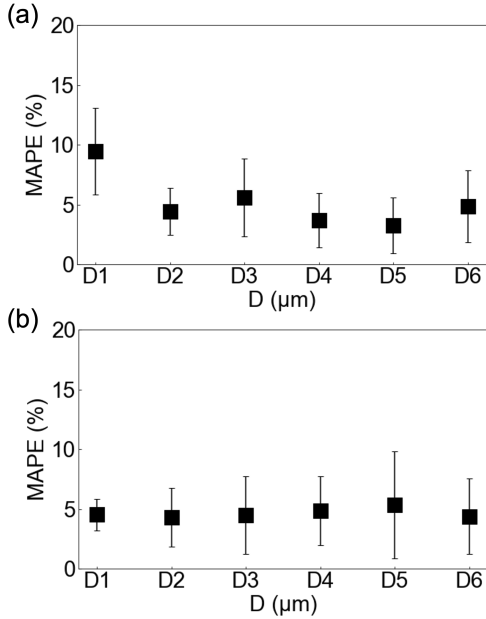

Fig. 4. Test MAPEs for each design: (a) R model and (b) H model. Error bars represent one standard deviation.

The extrapolation performance of the R and H models can be revealed by analyzing the MAPE values for D1 and D6 in Fig. 4. The test MAPE value of D1 for the R model is slightly larger compared with other hemisphere dimensions, indicating a potential limitation in the model's extrapolation ability at D1. On the other hand, the test MAPE value of D6 is comparable to D2–D5, suggesting an excellent extrapolation performance. The H model demonstrates outstanding extrapolation performance, which is evidenced by the fact that the MAPE
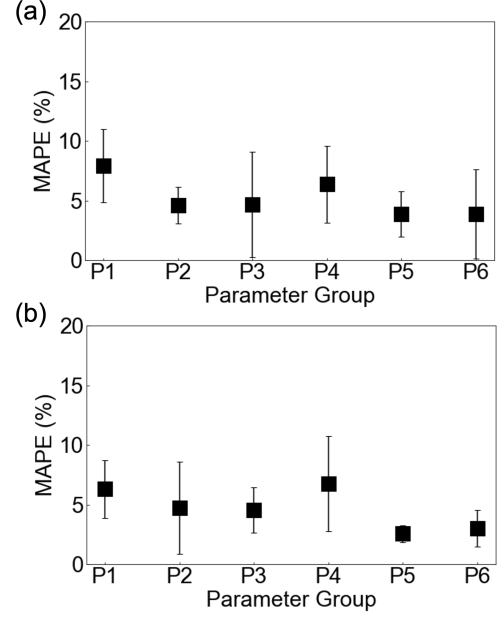

Fig. 5. Test MAPEs for each parameter group: (a) R model and (b) H model. Error bars represent one standard deviation.

values of D1 and D6 are comparable to other designs. It is worth noting that in both Fig. 4 and Fig. 5, each MAPE value and the associated error bar are calculated from six values. Differences in MAPEs are observed, which may suggest that the proposed models do not fully capture the variations caused by unknown physics. Another possible explanation is that the TPL machine suffers from some instability that causes natural variations [7].

5. Conclusion

In this paper, a physics-informed, data-driven modeling framework is developed for predicting the geometric compliance in TPL in a generalizable fashion. Building from physics-based modeling of voxel dimensions, the model is constructed as a function of LP and SR. The model parameters depict a strongly linear relationship across different hemisphere dimensions, which enables generalizable predictive modeling. The framework is shown to be highly effective in geometric accuracy prediction—the prediction error is less than 5% for both average height and equivalent radius features. To the best of our knowledge, this paper is among the first to develop an effective method for generalizable modeling of TPL geometric compliance cross process parameters and designs.

The results of this paper suggest three future research directions. First, it is interesting and important to investigate the uncaptured variations as indicated in Fig. 4 and Fig. 5. The proposed modeling framework can be extended to characterize such variations, e.g., by adding more modeling terms. Second, we plan to further demonstrate the generalizability of the framework by studying structures at different scales. This research demonstrates good generalizability over a range of 1 µm,

i.e., 1.6–2.6 μm. Future efforts can be devoted to investigating whether similar cross-design relationships exist at smaller and larger scales. Third, we will extend the proposed approach for predicting different and more complicated shape designs. Since TPL fabricates structures by stacking voxels, geometric features in x and z directions should follow similar patterns. Transfer learning techniques [10] may be required to capture both the similarities and differences between shape designs.

Acknowledgments

References

[1] V. Harinarayana *et al.*, "Two-photon lithography for three-dimensional fabrication in micro/nanoscale regime: A comprehensive review," *Opt. Laser Technol.*, vol. 142, p. 107 180, 2021.

[2] A. Vyatskikh *et al.*, "Additive manufacturing of 3d nano-architected metals," *Nat. Commun*, vol. 9, no. 1, pp. 1–8, 2018.

[3] G. Williams *et al.*, "Two-photon lithography for 3d magnetic nanostructure fabrication," *Nano Res.*, vol. 11, no. 2, pp. 845–854, 2018.

[4] D. Tan *et al.*, "Reduction in feature size of two-photon polymerization using scr500," *Appl. Phys. Lett.*, vol. 90, no. 7, p. 071 106, 2007.

[5] Y. Liu, "Direct laser writing of functional 3d micro/nanostructures by two-photon polymerization for enhanced mechanical and electrical properties," Ph.D. dissertation, The University of Nebraska-Lincoln, 2018.

[6] T. Baldacchini, *Three-dimensional microfabrication using two-photon polymerization: fundamentals, technology, and applications*. William Andrew, 2015.

[7] Y. Yang *et al.*, "Machine-learning-enabled geometric compliance improvement in two-photon lithography without hardware modifications," *J. Manuf. Process.*, vol. 76, pp. 841–849, 2022.

[8] X. Zhou *et al.*, "A review on the processing accuracy of two-photon polymerization," *AIP Adv.*, vol. 5, no. 3, p. 030 701, 2015.

[9] M. Álvarez *et al.*, "Near-field lithography by two-photon induced photocleavage of organic monolayers," *Adv. Funct. Mater.*, vol. 20, no. 24, pp. 4265–4272, 2010.

[10] C. Shao *et al.*, "Improving machined surface shape prediction by integrating multi-task learning with cutting force variation modeling," *J. Manuf. Sci. Eng.*, vol. 139, no. 1, p. 011 014, 2017.